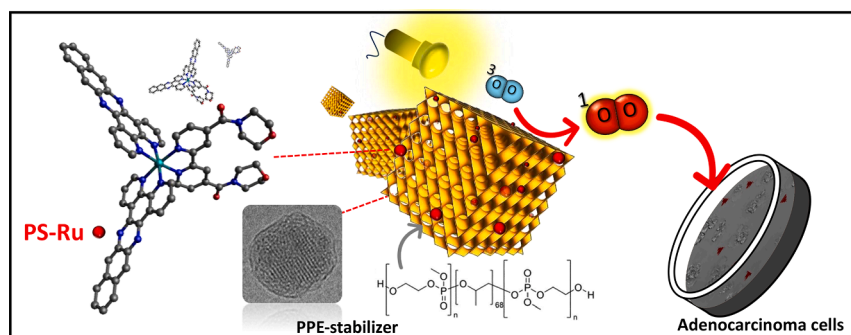Regular Article

Polyphosphoester-stabilized cubosomes encapsulating a Ru(II) complex for the photodynamic treatment of lung adenocarcinoma

Luca Casula [a,1], Gina Elena Giacomazzo [b,1], Luca Conti [b], Marco Fornasier [c,f], Benedetto Manca [d], Michele Schlich [a], Chiara Sinico [a], Timo Rheinberger [e], Frederik R. Wurm [e], Claudia Giorgi [b,*], Sergio Murgia [a,f,*]

[a] Department of Life and Environmental Sciences, University of Cagliari, Cittadella Universitaria Monserrato, S.P. 8 Km 0.700, 09042 Monserrato, CA, Italy
[b] Department of Chemistry "Ugo Schiff", University of Florence, via della Lastruccia 3, 50019 Sesto Fiorentino, FI, Italy
[c] Department of Chemistry, Lund University, SE-22100 Lund, Sweden
[d] Department of Mathematics and Computer Science, University of Cagliari, via Ospedale 72, 09124 Cagliari, CA, Italy
[e] Sustainable Polymer Chemistry (SPC), Department of Molecules and Materials, MESA+ Institute for Nanotechnology, Faculty of Science and Technology, University of Twente, P.O. Box 217, Enschede 7500 AE, Netherlands
[f] CSGI, Consorzio Interuniversitario per lo Sviluppo dei Sistemi a Grande Interfase, 50019 Sesto Fiorentino, FI, Italy

GRAPHICAL ABSTRACT

ARTICLE INFO

ABSTRACT

The clinical translation of photosensitizers based on ruthenium(II) polypyridyl complexes (RPCs) in photodynamic therapy of cancer faces several challenges. To address these limitations, we conducted an investigation to assess the potential of a cubosome formulation stabilized in water against coalescence utilizing a polyphosphoester analog of Pluronic F127 as a stabilizer and loaded with newly synthesized RPC-based photosensitizer [Ru(dppn)$_2$(bpy-morph)](PF$_6$)$_2$ (bpy-morph = 2,2′-bipyridine-4,4′-diylbis(morpholinomethanone)), PS-Ru. The photophysical characterization of PS-Ru revealed its robust capacity to induce the formation of singlet oxygen (^{1}O$_2$). Furthermore, the physicochemical analysis of the PS-Ru-loaded cubosomes dispersion demonstrated that the encapsulation of the photosensitizer within the nanoparticles did not disrupt the three-dimensional arrangement of the lipid bilayer. The biological tests showed that PS-Ru-loaded cubosomes exhibited significant phototoxic activity when exposed to the light source, in stark contrast to empty cubosomes and to the same formulation without irradiation. This promising outcome suggests the potential of the formulation in overcoming the drawbacks associated with the clinical use of RPCs in photodynamic therapy for anticancer treatments.

1. Introduction

Among the various applications of nanotechnology, nanomedicine has been a particularly well-explored area. Researchers in this field primarily aim to develop nanoparticles that are both safe and capable of precisely delivering drugs and imaging agents to pathological tissues. This approach seeks to maximize therapeutic effects while minimizing side effects, aligning with the goals of personalized medicine. However, despite substantial efforts, only a few nanomedicines have successfully been translated from the laboratory to the market. One key challenge contributing to this limited success is the insufficient biocompatibility of certain nanoparticle formulations.

Cubosomes represent a type of soft nanoparticles characterized by a lyotropic liquid crystalline bicontinuous cubic core [1,2]. Created by harnessing the natural self-assembly properties of various lipids (such as monoolein, MO, or phytantriol) in aqueous environments, they possess an inner structure consisting of a three-dimensional, curved, non-intersecting lipid double layer that extends throughout space, superimposed over an infinite periodic minimal surface (IPMS) with cubic symmetry, being the primitive (body-centered lattice, Im3m), the double gyroid (body-centered lattice, Ia3d), and the double diamond (primitive lattice, Pn3m), the most important in lipid-based systems. This unique structure results in the formation of two separate water channels. Because cubosomes can accommodate hydrophobic drugs and imaging probes, they are proposed for theranostic applications and, more broadly, for drug delivery purposes [3–5]. Cubosome dispersions are only kinetically stable and a dispersant is required to stabilize the nanoparticles against flocculation. Generally, the dispersant belongs to the family of non-ionic tri-block copolymers known as Pluronics, with F127 being the most representative. However, Pluronics are not biodegradable *in vivo* and can activate the complement system in the bloodstream, potentially causing cardiopulmonary distress in sensitive individuals. Rarely, other dispersants have been reported for stabilizing cubosomes in water, leading to the production of less cytotoxic formulations [6,7]. One of such dispersants is a recently synthesized polyphosphoester (PPE, a polyester based on phosphoric acid derivatives) analog of Pluronic F127, having the remarkable trait of being highly stable yet degradable when required. PPEs have received increased attention as biodegradable alternatives to polyethylene glycol (PEG), with similar antifouling [8] and blood compatibility [9] properties but adjustable hydrolysis rates [10]. Specifically, used as stabilizers, PPEs were found to improve the biocompatibility of cubosomes with respect to Pluronic F127. Well-defined PPE-block copolymers can be synthesized by metal-free, ring-opening polymerization providing fast access to degradable Pluronic alternatives.

Among the different active ingredients that can be incorporated into cubosomes, photosensitizer molecules (PS) are attracting increasing attention due to encouraging outcomes of photodynamic therapy (PDT)

in the treatment of different typologies of cancers, such as skin, lung and bladder cancer [11,12], as well as bacterial infections [13–15]. The possibility to activate the PS (acting as a prodrug) by using light represents indeed a crucial advantage, as it allows to deliver the phototoxic activity towards a desired target in a spatio-temporal manner, avoiding the heavy side effects normally incurring with standard therapeutics. This key feature is also typically associated with the high efficiency arising from the catalytic production of reactive oxygen species (ROS), such as the highly potent singlet oxygen ^{1}O$_2$ [16], making PDT an appealing resource, even when compared to the more recent photo-activated chemotherapy (PACT) approach [17–19]. Moreover, PDT-generated ROS can stimulate anti-tumor immune responses (in contrast to chemotherapy/radiotherapy) [20]. It is therefore surprising that PDT has not been broadly applied in clinic yet [21–23], being only intended for certain dermatological treatments [24,25]. The PS is one of the three ingredients of PDT along with light and availability of oxygen. Hydrophobicity, self-aggregation, low cell/tissue specificity and inadequate pharmacokinetics of PSs are crucial issues that are not compatible with systemic administration. Over the past years great interest has been focused on ruthenium(II) polypyridyl complexes (RPCs), a versatile class of compounds whose rich chemical-physical repertoire includes good ROS sensitizing properties, access to a variety of excited-state electronic configurations and the ability to interact with key biological targets (such as DNA or proteins) [26–31]. Moreover, their photochemical and photobiological properties can be finely modulated by an optimal choice of ligands in their octahedral geometries [32]. Of particular relevance are those RPCs containing the popular benzo[*i*]dipyrido[3,2-*a*:2′,3′-*c*] phenazine (dppn) ligand, a π-expansive ligand which imparts augmented ^{1}O$_2$ sensitizing properties, *via* the population of long-lived intraligand ^{3}IL states (^{3}ππ*), but even confers red-shifted absorption profiles and strengthens the DNA-interaction capabilities [33].

Adenocarcinoma of the lung, which is the most common type of non-small cell lung cancer (NSCLC), is a possible target for PDT. Despite a reduction in incidence and mortality over the last few decades, lung cancer is still responsible for the highest number of cancer deaths [34]. Lung adenocarcinoma may be treated with PDT using a minimally invasive procedure that includes systemic administration of the PS and subsequent photoirradiation of cancerous tissue through a fiberoptic bronchoscope. In addition to the lower invasiveness compared to surgery, PDT is significantly safer than other treatment modalities as it has targeted effects on the irradiated tissue, reducing the systemic toxicity typically associated with chemotherapy [35]. Photofrin®, the first clinical PDT for lung cancer, was approved in several countries in 1993 (in 1998 by the US FDA) and still represent a crucial alternative for patients bearing unresectable cancers (over 70 % of cases at diagnosis) for whom radiotherapy is not indicated [36]. Research and development of more potent PS and appropriate delivery (nano)vehicles would broaden the list of therapeutic options for such patients, allowing to

reduce the dose and improve the tissue selectivity.

Herein, we report on the physicochemical and biological aspects of a PPE-stabilized cubosome formulation encapsulating a newly synthesized photosensitizer [Ru(dppn)$_2$(bpy-morph)](PF$_6$)$_2$ (PS-Ru) (bpy-morph = 2,2′-bipyridine-4,4′-diylbis(morpholinomethanone)), potentially applicable for the photodynamic treatment of lung adenocarcinoma (Fig. 1).

2. Experimental

2.1. Materials

All solvents were purchased in HPLC grade or dry (purity > 99.8 %) and chemicals were purchased in the highest grade (purity > 98 %) from Sigma Aldrich, Acros Organics, Fluka VWR chemicals or Fisher Scientific and used as received unless otherwise described. Poly(propylene oxide) molar mass 4,000 g mol^{-1} were purchased from Sigma Aldrich (the KOH impurities were removed by extraction in dichloromethane with water) the pure and dry polymer was freeze dried with benzene and stored under nitrogen atmosphere. 1,8-Diazabicyclo[5.4.0]undec-7-ene (DBU) was distilled from calcium hydride and stored over molecular sieves (3 and 4 Å) under a nitrogen atmosphere. *N*-Cyclohexyl-N′-(3,5-bis(trifluoromethyl)phenyl)thiourea (TU) was synthesized according to the procedure described by Tripathi *et al.* [37] 2-methoxy-2-oxo-1,3,2-dioxaphospholane (MEP) was synthesized according to the procedure described by Steinbach *et al.* [38].

Benzo[*i*]dipyrido[3,2-*a*:2′,3′-*c*]phenazine (dppn) was prepared according to literature procedures [39], through Schiff-base condensation reaction of 1,10-phenanthroline-5,6-dione with commercially available 2,3-diaminonaphtalene. The polymeric precursor [Ru(CO)$_2$Cl$_2$]$_n$ was prepared by reaction of RuCl$_3$·nH$_2$O with crystalline paraformaldehyde in formic acid 90 %. Following 6 h at reflux excluding light, [Ru(CO)$_2$Cl$_2$]$_n$ was isolated as a pale-yellow powder through trituration from hexane [40]. The Ru(II)-intermediates *trans*-Cl[Ru(bpy-morph)(CO)$_2$Cl$_2$] was obtained through slight modifications of procedures reported in literature [40,41], following reaction between the polymeric precursor [Ru(CO)$_2$Cl$_2$]$_n$ and bpy-morph in 1.1:1 M ratios in refluxing methanol and direct obtaining of the ruthenium intermediate by hot filtration from the reaction mixture. Ru(II) complex PS-Ru is chiral and was isolated as a racemic mixture of Δ and Λ enantiomers. No attempts to obtain the pure enantiomers were made in this work.

For cubosomes preparation, monoolein (MO, 1-monooleoylglycerol, RYLO MG 19 PHARMA, 98.1 wt%), was kindly provided by Danisco A/S (Denmark). The samples were prepared using fresh distilled water purified using a MilliQ system (Millipore) and filtered with a 0.22 μm pore size hydrophilic filter.

2.2. Nuclear magnetic resonance (NMR) spectroscopy

The ^{1}H, and ^{31}P NMR spectra were measured on a 400 MHz *Bruker AVANCE III AMX* system. The temperature was kept at 298.3 K. As deuterated solvent CDCl$_3$ was used. For analysis of all measured spectra MestReNova 9 from Mestrelab Research S.L. was used. The spectra were calibrated against the solvent signal.

2.3. Synthesis of 2,2′-bipyridine-4,4′-diylbis(morpholinomethanone) (bpy-morph)

A catalytic amount of dimethylformamide (a drop) was added to a suspension of 2,2′-bipyridine-4,4′-carboxylic acid (dcbpy, 500 mg, 2.04 mmol) in 6 mL of thionyl chloride [42]. The reaction mixture was stirred at reflux for 4 h under N$_2$ atmosphere. After cooling at r.t., thionyl chloride was co-evaporated with toluene, and the red residue was immediately suspended in 10 mL of dry tetrahydrofuran. Potassium carbonate (860 mg, 6.15 mmol) and morpholine (179 mg, 4.10 mmol) were added, the reaction mixture was stirred at r. t. overnight under N$_2$ atmosphere and then filtered on a Celite pad washing with chloroform. The solution was washed three times with water and once with brine. The organic phase was dried on Na$_2$SO$_4$ and evaporated to dryness. bpy-morph was obtained as a pale-yellow powder (294 mg, 0.77 mmol) with a yield of 38 % over two reaction steps.

^{1}H NMR (400 MHz, CDCl$_3$): δ 8.80 (d, J = 4.8 Hz, 2H, **H$_{6/6'}$**), 8.49 (s, 2H, **H$_{3/3'}$**), 7.41 (d, J = 4.8, 2H, **H$_{5/5'}$**), 3.86 (bs, 8H, –CH$_2$ morpholine), 3.70 (bs, 4H, –CH$_2$ morpholine), 3.49 (bs, 4H, –CH$_2$ morpholine) ppm. ^{13}C NMR (100 MHz, CDCl$_3$): δ 168.3, 156.1, 150.4, 145.0, 122.5, 119.5, 67.4, 48.5, 43.0 ppm.

2.4. Synthesis of trans-Cl[Ru(bpy-morph))(CO)$_2$Cl$_2$]

To a solution of the polymeric precursor [Ru(CO)$_2$Cl$_2$]$_n$ (150 mg, 0.64 mmol) in 11 mL of dry methanol was added bpy-morph (221 mg, 0.58 mmol) and the reaction mixture was hated to reflux and stirred under N$_2$ atmosphere for 2 h excluding light. The precipitate was filtered hot and washed with methanol to obtain complex *trans*-Cl[Ru(bpy-morph)(CO)$_2$Cl$_2$] as yellow solid with a yield of 74 %.

^{1}H NMR (400 MHz, (CD$_3$)$_2$SO): δ 9.34 (d, J = 5.6, 2H, **H$_{6/6'}$**), 8.93 (s, 2H, **H$_{3/3'}$**), 7.90 (d, J = 5.2, 2H, **H$_{5/5'}$**), 3.73 (s, 8H, –CH$_2$ morpholine), 3.62 (s, 4H, –CH$_2$ morpholine), 3.36 (s, 4H, –CH$_2$ morpholine) ppm. ^{13}C
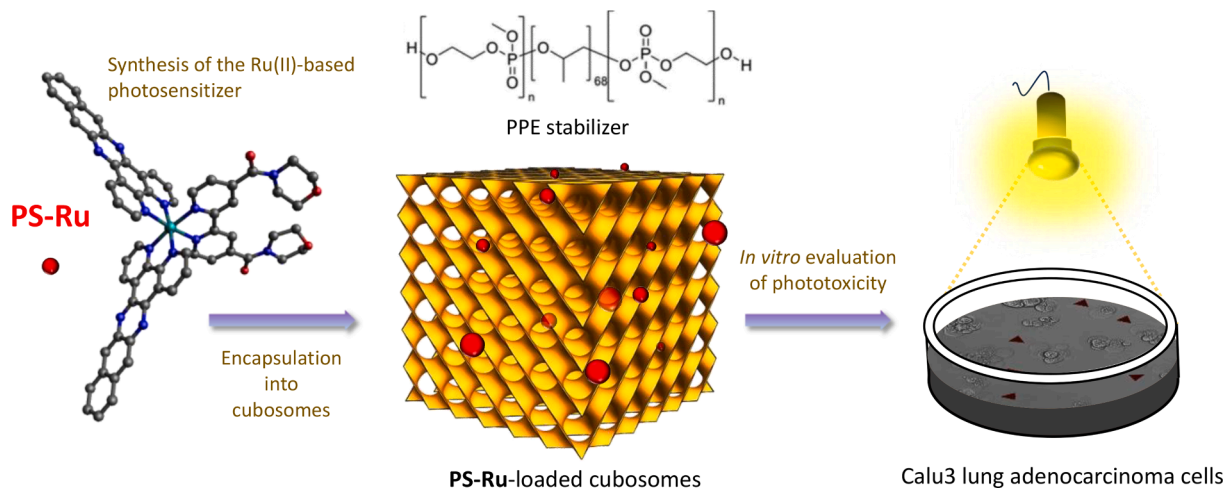

Fig. 1. Conceptual scheme of the photosensitizer-loaded cubosomes formulation here presented and its application. Cubosomes are represented through their IPMS of Pn3m symmetry (see Introduction and Experimental sections).

NMR (100 MHz, (CD$_3$)$_2$SO): δ 197.0, 171.3, 166.0, 155.7, 155.6, 154.9, 148.2, 126.6, 123.5, 67.0, 66.8, 48.4, 43.0 ppm.

2.5. Synthesis of ruthenium complex [Ru(dppn)$_2$(bpy-morph)](PF$_6$)$_2$ (PS-Ru)

To a solution of *trans*-Cl[Ru(bpy-morph))Cl$_2$(CO)$_2$] (100 mg, 0.16 mmol) in 8 mL of degassed 2-methoxyethanol, benzo[*i*]dipyrido[3,2-*a*:2′,3′-*c*]phenazine (dppn, 106 mg, 0.32 mmol) and trimethylamine *N*-oxide (TMAO, 116 mg, 1.04 mmol) were added. The reaction mixture was stirred for 4 h at reflux under N$_2$ atmosphere. After cooling at r.t., the addition of 2 mL of 0.1 M of KPF$_6$ aqueous solution allowed the complete precipitation of the ruthenium complex as the hexafluorophosphate salt PS-Ru. The crude product was filtered and washed with water, methanol, and diethyl ether. Successively, PS-Ru was purified through flash chromatography on silica gel (eluent: dichloromethane:methanol 30:1 with 10 % acetone) to obtain complex PS-Ru as red solid with a yield of 62 %.

^{1}H NMR (400 MHz, (CD$_3$)$_2$CO): δ 9.83 (d, J$_{c-b}$ = 8 Hz, 2H, **H$_c$**), 9.74 (d, J$_{c′-b′}$ = 8 Hz, 2H, **H$_{c′}$**), 9,22 (s, 2H, **H$_d$**), 9.18 (s, 2H, **H$_{d′}$**), 8.98 (s, 2H, **H$_{3/3′}$**), 8.76 (d, J$_{a-b}$ = 4 Hz, 2H, **H$_a$**), 8.62 (d, J$_{a′-b′}$ = 4 Hz, 2H, **H$_{a′}$**), 8.48–8.40 (m, 6H, **H$_{6/6′}$, H$_e$/H$_{e′}$**), 8.15 (dd, J$_{b-c}$ = 4 Hz, J$_{b-a}$ = 8 Hz, 2H, **H$_b$**), 7,97 (dd, J1$_{b′-c′}$ = 4 29 Hz, J2$_{b′-a′}$ = 8 Hz, 2H, **H$_{b′}$**), 7.85–7.79 (m, 4H, **H$_f$/H$_{f′}$**), 7.53 (d, J H$_3$-H$_2$ = 4 Hz, 2H, **H$_{5/5′}$**), 3.71 (bs, 8H, –CH$_2$ morpholine), 3.60 (bs, 4H, –CH$_2$ morpholine), 3.50 (bs, 4H, –CH$_2$ morpholine) ppm. ^{13}C NMR (100 MHz, (CD$_3$)$_2$CO): δ 166.0, 158.6, 155.4, 155.0, 153.6, 152.0, 146.0, 141.6, 141.5, 139.3, 139.2, 135.9, 134.7, 134.6, 132.0, 131.9, 129.3, 129.2, 128.9, 128.8, 128.7, 128.6, 128.3, 126.0, 123.5, 67.0, 66.7, 48.2, 42.7 ppm. HR-MS (ESI +) *m/z*: calcd. for C$_{64}$H$_{46}$N$_{12}$O$_4$Ru [M−2PF$_6^-$]$^{2+}$ 574.13987, found: 574.13897. Combustion elemental analysis calculated for C$_{64}$H$_{46}$N$_{12}$F$_{12}$O$_4$P$_2$Ru: C 53.45, N 11.69, H 3.22; found C 53.28, N 11.04, H 3.42.

2.6. Singlet oxygen quantum yield determination

The quantum yield for ^{1}O$_2$ generation (ϕ_Δ) by PS-Ru was determined by direct measurement of the phosphorescence signal of O$_2$($^1\Delta_g$) $\rightarrow$ ^{3}O$_2$ at 1270 nm, following irradiation at 440 nm in air-saturated acetonitrile solutions. Experiments were carried out on solutions of the photosensitizer at different concentrations, with the ^{1}MLCT absorbance values ranging between 0.08 and 0.2. Phosphorescence signals were collected by using a N$_2$ cooled InGaAs photodiode, on a spectrophotofluorimeter Horiba FluoroMax. ϕ_Δ values were determined as previously described, by comparison with [Ru(phen)$_3$]$^{2+}$ taken as reference compound for ^{1}O$_2$ sensitization (ϕ_Δ = 0.38 $\pm$ 0.06) [43].

2.7. Characterization of intermediates and of the of ruthenium complex PS-Ru

The ^{1}H, ^{13}C NMR, COSY and HSQC spectra were collected with a Bruker 400 MHz spectrometer. UV–Vis absorption spectra were acquired on a Perkin-Elmer Lambda 6 spectrophotometer. Fluorescence spectra and measurements of the phosphorescence signal of ^{1}O$_2$ were carried out on a spectrofluorometer Horiba FluoroMax Plus.

2.8. Polymerization of 2-methoxy-2-oxo-1,3,2-dioxaphospholane (MEP)

The polyphosphoester (PPE) Pluronic mimic was synthesized according to a previously reported method [44]. TU (260 mg, 7.0·10^{-4} mol) and the poly(propylene oxide)$_{68}$-macroinitiator (225,7 mg, 5.6 10^{-5} mol PPO-diol of molar mass 4,000 g mol^{-1}) were placed in a Schlenk tube and freeze-dried with benzene prior use. MEP (1.65 g, 1.20·10^{-2} mol) were freeze-dried with benzene in a separate Schlenk tube, then dissolved in 3 mL of dry dichloromethane and added to the initiator mixture. The solution was cooled down to -10 °C, then the polymerization was initiated by the rapid addition of 2.70 mL of 0.2 mol/L DBU

in dichloromethane (55 mg, 3.6·10^{-4} mol) to the stirred solution. The polymerization was terminated after 3 h by the addition of ca. 1 mL acetic acid in dichloromethane (20 mg mL^{-1}). The polymer was purified by precipitation from dichloromethane into ice-cold diethyl ether twice, followed by dialysis against deionized water overnight (MWCO: 3500). The polymer was obtained after freeze-drying in quantitative yield.

1H NMR (CDCl3, ppm): δ = 4.62 – 4.09 (m, MEP backbone –CH2-), 3.80 (d, 3JHP = 11.2 Hz, MEP side-chain-O-CH3), 3.62 – 3.28 (m, PPO backbone), 1.24 – 1.03 (m, PPO side-chain –CH3), 31P NMR (CDCl3, ppm): δ = -0.2 (see SI, Fig S15).

2.9. Cubosomes preparation

Cubosomes were prepared using a dry thin film method. MO and PS-Ru were firstly dissolved in DCM at 40 °C in a glass tube. The solvent was then evaporated by rotary evaporation (Rotavapor, Buchi, Germany) to obtain a dry thin film. The sample was kept under vacuum to remove final traces of solvent, and then frozen overnight. The obtained dry films were hydrated with an appropriate amount of a PPE water solution, with the help of an ultrasonic bath. The mixture was ultrasonicated using a UP100H ultrasonic processor developed by Hiescher (Hielscher Ultrasonics GmbH, Germany) (amplitude 90 %; 1 s ON, 1 s OFF) for 5, 4, 3, 2, and 1 min cycles. The cubosome formulation investigated had a composition of MO/PPE/PS-Ru = 3.3/0.3/0.025 % (w/w). The PS-Ru-loaded cubosomes were then separated from the free PS-Ru by dialyzing the formulation using a tubing cellulose membrane (14 kDa molecular weight cutoff, Sigma Aldrich) against 2 L of water for 2 h (water was changed after 1 h) at room temperature. To evaluate the drug entrapment efficiency, after cubosomes disruption in methanol, a Synergy 4 multiplate reader (BioTek, Winooski, USA) was used for the quantitative determination of PS-Ru by means of UV–Vis spectroscopy at 460 nm. The encapsulation/entrapment efficiency (EE%) was calculated exploiting the following expression:

$$EE\% = \frac{mass\ of\ drug\ after\ dialysis}{mass\ of\ weighted\ drug} \, x\, 100\%$$

Empty cubosomes (ECub) were prepared as control, using the same technique without any PS compound.

2.10. Small angle X-ray scattering

The structure of the cubosomes loaded with PS-Ru was investigated by means of Small Angle X-ray Scattering (SAXS). The measurements were performed in a SAXSLab Ganesha instrument (JJ-Xray, Denmark), equipped with a 30 W Cu X-ray micro-source (Xenocs, France) and a 2D 300 K Pilatus detector (Dectris, Switzerland). The data were acquired with a pin-hole collimated beam with the detector positioned asymmetrically at a distance of 480 mm from the sample, to yield azimuthally averaged intensities as a function of the scattering vector (q), over the range 0.012 – 0.67 Å^{-1}. The magnitude of the scattering vector is defined by $q = (4\pi sin\theta)/\lambda$, where λ equals to 1.54 Å (Cu Kα wavelength) and θ is half of the scattering angle.

The cubosomes dispersion was loaded in 1.5 mm quartz capillary cells and placed in a thermostat stage at 25 °C, controlled using a Julabo T Controller CF41 (Julabo Labortechnik GmbH, Germany, and equilibrated for 1800 s before any SAXS measurements.

The d spacing was obtained from the positions of the Bragg peaks detected in the patterns (q_{peak}) by the following expression:

$$d = \frac{2\pi}{q_{peak}}$$

Then, the lattice parameter of the liquid crystalline phase structure, a, was calculated for the bicontinuous cubic using the following equation

$$a = d \bullet \sqrt{h^2 + k^2 + l^2}$$

where *h*, *k* and *l* are the Miller indexes that describe the crystalline planes of lattice. The lattice parameter was used to evaluate the water channel radius (r_w) of the bicontinuous cubic phase as follows:

$$r_w = (a - l) \bullet \sqrt{\frac{A_0}{-2\pi\chi}}$$

where χ and A_0 are, respectively, the Euler characteristic and the surface area of the IPMS geometry (Pn3m, $\chi = -2$, $A_0 = 1.919$), and *l* is the monoolein hydrophobic chain length at 25 °C (17 Å) [45].

The *q* scale was calibrated using silver behenate (CH_3–$(CH_2)_{20}$-COOAg) as a standard.

The temperature scan measurements were performed at 25, 37, 10 and then back to 25 °C by letting the samples equilibrating for two hours at each temperature, to ensure thermal equilibrium.

2.11. Graphic representation of the Pn3m IPMS

The Pn3m IPMS (Infinite Periodic Minimal Surface) depicted in Fig. 1 as pictorial representation of a cubosome is obtained exploiting the fact that such minimal surface is given by the zeros of the following function [46]:

$$f(x,y,z) = \sin(x) \bullet \sin(y) \bullet \sin(z) + \sin(x) \bullet \cos(y) \bullet \cos(z) + \cos(x) \\ \bullet \sin(y) \bullet \cos(z) + \cos(x) \bullet \cos(y) \bullet \sin(z)$$

The 3D plot is produced using the function ContourPlot3D from the software Wolfram Mathematica [47] by considering the variables x,y,z inside the interval $[-3\pi, +3\pi]$.

2.12. Dynamic and electrophoretic light scattering

The apparent hydrodynamic diameter (D_h), the polydispersity index (PdI) and the zeta potential of the cubosomes were estimated via Dynamic Light Scattering (DLS) and Electrophoretic Light Scattering (ELS), respectively.

DLS measurements were performed in a ZetaSizer Nano ZS by Malvern Panalytical set in a backscattering geometry at a fixed scattering angle of 173°. The cubosomes were diluted 1:50 in water and analyzed in disposable cuvettes. The values of the intensity-weighted D_h and polydispersity index were extracted from a second order Cumulant analysis. The parameters were collected from at least six independent measurements of 10 runs each.

The electrophoretic mobilities were collected at a fixed scattering angle of 17° using laser Doppler electrophoresis method with disposable folded capillary cells (DTS1070). Zeta potential values were estimated from electrophoretic mobility data by using Smoluchowski's equation and stated as the average of three consecutive measurements.

Both DLS and ELS measurements were performed leaving the samples equilibrating at 25, 37, 10 and then back to 25 °C for 1 h.

Additionally, the formulation was tested for a medium-term stability study at 25 °C, with D_h, PdI, and zeta potential of cubosomes being monitored for a duration of 30 days. Before each DLS and ELS measurement, the samples were visually examined to make sure there were no large aggregates or phase separation.

2.13. Cryogenic transmission electron microscopy

The morphology of the cubosomes loaded with the novel photosensitizer was imaged via cryogenic transmission electron microscopy (cryo-TEM) at the National Center for High Resolution Electron Microscopy (nCHREM) at Lund University. The JEM-2200FS transmission electron microscope (JEOL) was equipped with a field-emission electron source, a cryo-pole piece in the objective lens and an in-column energy filter (omega filter). The recording of zero-loss images was acquired at

an acceleration voltage of 200 kV on a bottom-mounted TemCam-F416 camera (TVIPS) using SerialEM under low-dose conditions. The sample was vitrified before measuring using an automatic plunge freezer system (Leica Em GP) in an environmental chamber at 25.0 °C and 90 % of relative humidity. A 4 μL droplet of the dispersions of the formulation was deposited on a lacey formvar carbon-coated grid (Ted Pella), and the excess liquid was removed with filter paper after blotting. The grids were plunged into liquid ethane (around –183 °C), ensuring rapid vitrification of the cubosomes in their native state. Each grid was stored in liquid nitrogen (–196 °C) prior to any imaging session, and then transferred into the microscope using a cryo-transfer tomography holder (Fischione, Model 2550).

2.14. In vitro activity of PS-Ru and PS-Ru-loaded cubosomes

The human lung adenocarcinoma cell line Calu-3 was purchased by ATCC and grown in Dulbecco's Modified Eagle Medium (DMEM, High Glucose), supplemented with 10 % fetal bovine serum, Penicillin/Streptomycin (50 units/mL each), sodium pyruvate (1 mM) and non-essential amino acids (1 mM). Cells were seeded onto 96 well plates at a density of $2x10^4$ cells/well and allowed to attach and grow for 24 h in 95 % humidified atmosphere with 5 % CO_2 at 37 °C. Cells were then treated with PS-Ru (solubilized in DMSO), empty cubosomes or PS-Ru-loaded cubosomes diluted in complete medium (0.025–25 μM). After 1 h incubation, the medium was replaced, and cells were either exposed to LED light for 30 min employing a customized cell illumination device (λmax = 462 nm, 18 mW cm^{-2}) [48] or incubated in the dark. Both groups were further cultured for 24 h before replacing the medium with 3-(4,5-dimethylthiazolyl)-2,5-diphenyltetrazolium bromide (MTT) (0.25 mg/ml). After 3 h, the medium was replaced with ethanol and optical density (OD) of wells was recorded on a plate reader (Synergy 4, BioTek) at 570 nm. The OD values were used to calculate the percentage of viable cells in each well, setting the OD of untreated cells (without PS and not exposed to light) as 100 %. Each condition was tested in 5 replicates. Cells were observed by light microscopy using a Leica DM IL LED equipped with 20x objective. Images were acquired by a Leica MC170 HD camera controlled by LAS V4.12 software.

3. Results and discussion

3.1. Synthesis, characterization and singlet oxygen sensitizing properties of PS-Ru

The synthesis of the ruthenium-based photosensitizer (PS-Ru) was accomplished by a straightforward synthetic method recently reported by our group [48] for the obtaining of bis-heteroleptic RPCs of the general formula [Ru(dppn)$_2$L]$^{2+}$ (L = bidentate polypyridyl chelates) and illustrated in Fig. 1.

Compared to the most commonly employed synthetic route for complexes of the family [Ru(NN)$_2$L]$^{2+}$ (NN = polypyridyl bidentate ligand) [49,50], the main advantage of this "reverse" approach consists in the insertion of two dppn ligands into the Ru(II)-scaffold only in the last step of reaction. This is of outmost importance as it permits to avoid the use of the [Ru(dppn)$_2$Cl$_2$] intermediate, which is scarcely soluble in most organic solvents and has therefore represented a central issue responsible for the net discrepancy between the numerous mono-, and the much rarer di-, dppn containing RPCs developed so far.

As shown in Fig. 2, for the preparation of PS-Ru herein the 2,2′-bipyridine-4,4′-diylbis(morpholinomethanone) ligand (bpy-morph) was first obtained by reacting two equivalents of morpholine in dry THF with the intermediate 2,2′-bipyridine-4,4′-dicarbonyl dichloride, which was in turn obtained by refluxing the commercially available 2,2′-bipyridine-4,4′-carboxylic acid (dcbpy) in thionyl chloride. Then, the bpy-morph ligand was allowed to react with the polymeric precursor [Ru(CO)$_2$Cl$_2$]$_n$ in refluxing methanol affording *trans*-Cl[Ru(bpy-morph)(CO)$_2$Cl$_2$] upon hot filtration from the reaction mixture, by performing
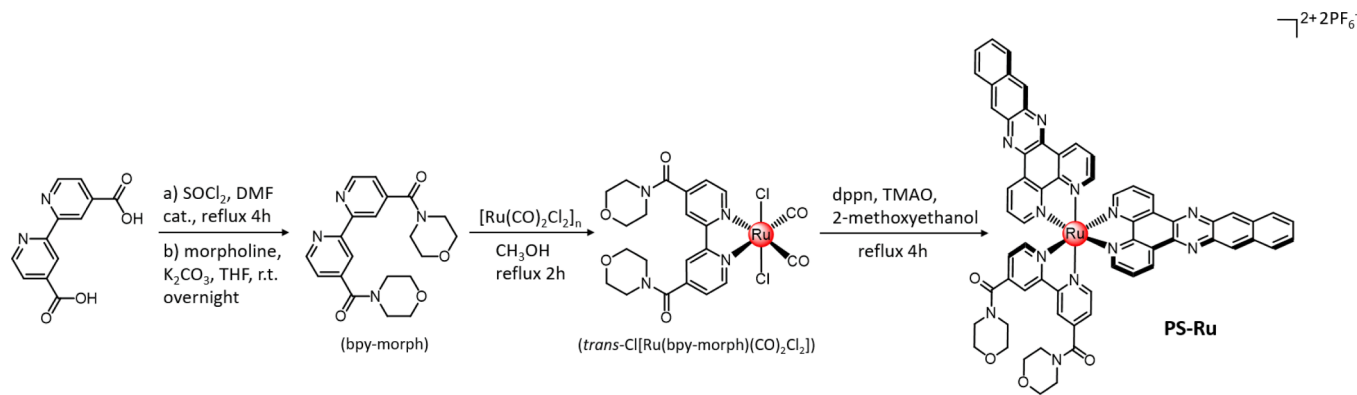
Fig. 2. Synthetic route followed for the preparation of the ruthenium photosensitizer PS-Ru.

slight modifications of procedures reported in literature [40,41].

Lasty, two equivalents of dppn were added to a solution of *trans*-Cl [Ru(bpy-morph)(CO)$_2$Cl$_2$] in 2-methoxyethanol and in the presence of trimethylamine *N*-oxide (TMAO), the latter being used to facilitate the detachment of the strongly coordinated CO ligands and favor their replacement by the bidentate dppn ligands [51]. Addition of aqueous KPF$_6$ led to the precipitation of the hexafluorophosphate salt PS-Ru, which was obtained in a yield of 62 % after purification through flash chromatography.

The identity of the obtained compounds was confirmed by ^{1}H, ^{13}C, COSY and HSQC NMR and high-resolution mass spectrometry (HR-MS) analysis (see SI, Fig. S1-S13).

The electronic absorption and fluorescence spectra collected for PS-Ru in acetonitrile are reported Fig. 3A.

As shown, besides the intense intraligand $\pi \rightarrow \pi^*$ transitions at 280–330 nm, PS-Ru displays a characteristic double humped absorption centered at $\sim$ 385 and $\sim$ 409 nm, which can be associated to the dppn centered $\pi \rightarrow \pi^*$ transitions, plus a broad ^{1}MLCT absorption around 460 nm, characteristic of analogues compounds reported in literature [52,53]. The complex also features a broad fluorescence emission in acetonitrile, with a maximum at 548 nm and a luminescence quantum yield (φ_L) in the order of 10^{-4} (see SI). This, along with the remarkable photosensitizing properties of the complex (*vide infra*), suggests that most of the energy of the excited photosensitizer is lost during the sensitization of singlet oxygen, in good agreement with what recently proposed for parental compounds [54]. A significant effect of the solvent
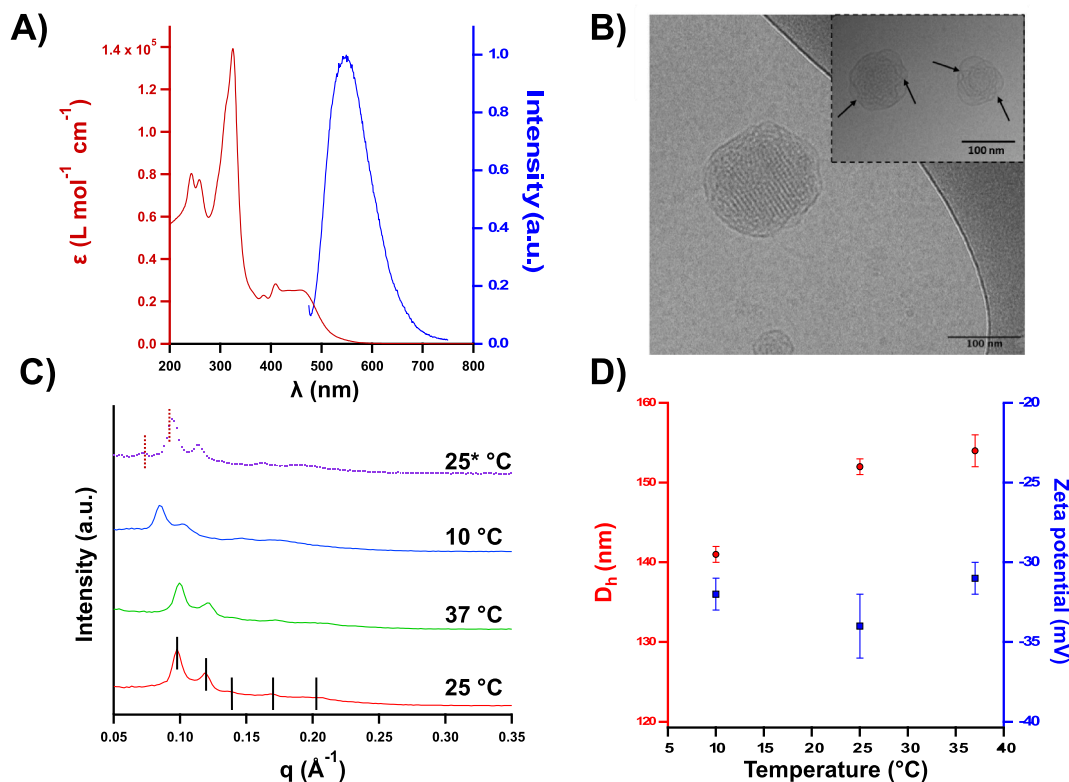

Fig. 3. A) Absorption and (normalized) emission spectra for the photosensitizer PS-Ru in acetonitrile ([PS-Ru] = 10 μM, λ$_{exc}$ 410 nm). B) Cryo micrographs of the PS-Ru-loaded cubosome formulation. The black arrows highlight the presence of ILAs. C) SAXS pattern of the formulation undergoing a temperature cycle scan. The Pn3m pattern is highlighted by the presence of the black lines on the peak maxima, whereas the presence of the Im3m is shown by the red dotted lines. The end of the heating/cooling cycle is denoted as with an asterisk. D) Average hydrodynamic diameters (red, left y-axis) and zeta potential (blue, right y-axis) of the sample as a function of temperature. The data are reported as average value ± standard deviation from three independent measurements. (For interpretation of the references to colour in this figure legend, the reader is referred to the web version of this article.)

on the emission profile of PS-Ru was also observed (Fig. S14-15, SI), as witnessed, for instance, by the strongly quenched and red-shifted emission registered in water compared to the one collected in acetonitrile; a comparison between the absorption and emission maxima values measured in acetonitrile and water is provided in Table 1.

Preliminary to the evaluation of the phototoxicity of a novel photosensitizer is the exploration of its ability to effectively sensitize the formation of singlet oxygen upon irradiation. The sensitization of such potent cytotoxic species represents indeed a crucial requisite by which a candidate PS can pursue its light-induced, biological activity based on *type II*-based cytotoxic pathways [55].

The singlet oxygen sensitizing properties of PS-Ru were inspected spectrophotometrically, by direct measurements of the phosphorescence signal of $^1O_2$ at 1270 nm, generated upon irradiation of air-saturated acetonitrile solutions of the ruthenium compound: the corresponding quantum yield of $^1O_2$ generation (ϕ_Δ) was then determined by comparison with the reference compound $[Ru(phen)_3]^{2+}$ and listed in Table 1. As shown, PS-Ru exhibits a potent ability to sensitize the formation of such harmful species, with a ϕ_Δ value of 0.54 ± 0.06, i.e., 42 % higher relative to the one of the reference standard ($\phi_\Delta = 0.38 \pm 0.06$) [43], confirming the beneficial role played the two π-expansive dppn ligands into the architecture of this PS.

3.2. Formulation and physicochemical characterization of PS-Ru-loaded cubosomes

To improve the potential biomedical application of the synthesized complex and address its low water solubility, a PS-Ru loaded cubosomes formulation (PS-RuCub) was designed using MO as molecular building block and PPE as a stabilizing agent. The fluid aqueous dispersions obtained had a milky macroscopic appearance, with cubosomes hydrodynamic diameters (D_h) of approximately 148 nm and 151 nm for, respectively, the PS-RuCub and an empty cubosomes formulation (ECub), used for comparison (Table 2). With PdI values less than 0.2, both formulations displayed a narrow size distribution, with slightly higher values in case of the ECub. Similarly, the zeta potential value recorded for ECub was only marginally higher compared to PS-RuCub, possibly because of the positive charge of the PS agent. The preparation of the samples using the dry thin film method led to a high encapsulation efficiency of PS-Ru (90 %), which was observed after dialysis and disruption of the nanoparticles. It deserves noticing that ECub and Ps-RuCub formulations discussed in this work were stabilized against coalescence using 0.6 wt% of PPE (Mn value of 33,000 g/mol), while Pluronic F127 (PF127)-stabilized cubosomes are typically prepared using not less than 0.3 wt% of PF127 (Mn value of 12,600 g/mol) (see also ref. 44), corresponding to a PPE/PF127 molar ratio of around 0.75.

The PS-RuCub dispersion was investigated under the physicochemical point of view to highlight if the inclusion of the ruthenium compound may affect morphology, inner structure, size, and stability of the nanocarrier.

First, cryo-TEM measurements were performed, and results of this analysis are shown in Fig. 3B. After blotting on the grid at 25 °C, the sample consisted of inner-structured quasi-spherical objects showing the

Table 1

Electronic absorption fluorescence emission maxima measured in acetonitrile and water, along with the quantum yield for $^1O_2$ generation (ϕ_Δ) determined in acetonitrile by direct measurements of the $^1O_2$ phosphorescence signal at 1270 nm.

Media	λ_{abs}/nm (ε x 10^3 M^{-1} cm^{-1})	$\lambda_{em}/\lambda_{exc}$ (nm)	ϕ_Δ ($^1O_2$)
CH₃CN	325 (138.1), 385 (22.9), 409 (28.3), 460 (25.3)	548/410	0.54 ± 0.06
water	325 (76.2), 389 (17.9), 412 (20.3), 460 (20.3)	636/410	—

Table 2

Cubosomes characterization in terms of apparent hydrodynamic diameter (D_h, nm), polydispersity index (PdI), zeta potential (mV) and encapsulation efficiency (EE%). Asterisk indicates samples incubated in DMEM cell culture medium.

	ECub	ECub*	PS-RuCub	PS-RuCub*
D_h (nm)	151 ± 3	148 ± 2	152 ± 2	146 ± 1
PdI	0.17 ± 0.03	0.12 ± 0.02	0.14 ± 0.01	0.10 ± 0.01
Zeta potential (mV)	− 39 ± 2	− 17 ± 2	− 34 ± 2	− 17 ± 1
EE%	—–	—–	90 ± 8	—–

honeycomb structure typical for cubosomes. Interestingly, numerous nanoparticles also show interlamellar attachments, or ILAs (indicated by the arrows in Fig. 3B), described in literature as fundamental intermediate states involved in the evolution from planar lamellar structures to the three-dimensional bicontinuous cubic assemblies [56,57] ILAs are often observed in cubosome formulations, and their concentration is usually proportional to the amount of the stabilizer used, typically a block co-polymer [5,58].

The morphology of the cubosomes is retained, as the structures highlighted in the micrographs are in line with others already reported in the literature for this composition without PS-Ru [44]. As a final remark, cryo-TEM analysis revealed that the sample is characterized by the absence of vesicles [4,59], often found also in high amount, in cubosome formulations (see also Fig. S17).

SAXS patterns (Fig. 3C) of the loaded formulations were then acquired at room (25 °C), body (37 °C) and storage (10 °C) temperature to highlight how this parameter may affect the structure of the cubosomes. The samples exhibited a Pn3m bicontinuous cubic pattern at 25 °C, typical of the formulation containing MO and the PPE as stabilizer [44], and encapsulation of PS-Ru did not influence the structure in a significant manner. The lattice parameters and the water channel radius, evaluated by the position of the peaks related to the Pn3m and Im3m patterns, are also in accordance with the ones previously reported for MO-based cubosomes (Table 3) [5].

When the temperature of the sample was increased to 37 °C, the peaks of the Pn3m phase shifted to higher scattering vector values, meaning that the lattice parameter and the water channel radius are decreasing. This is related to the higher thermal motion of the lipid chains that may assume different conformations and reduce the hydrophobic volume, leading to a smaller space occupied by this portion in the elementary cell of the Pn3m phase.

After cooling the cubosome formulation down to 10 °C, the peaks shifted towards lower q values, leading also to a higher lattice parameter and water channel radius. This is in accordance with a possible rearrangement of the tails of MO, where the chains are more elongated, thus occupying a bigger volume [45]. Interestingly, despite maintaining the original inverse bicontinuous cubic Pn3m phase when reducing the temperature from 25 to 10 °C, an unexpected decrease in the average hydrodynamic diameter of the nanoparticles is observed alongside an increase in lattice size (refer to Table 1 and Fig. 3D). This counterintuitive phenomenon may be attributed to the reduced mobility of the PPE hydrophilic arms, resulting in less protrusion into the bulk water. Consequently, although the lipid nanostructure swells, D_h diminishes

Table 3

Lattice parameters, *a*, and water channel radius, r_w, for the PS-RuCub cubosomes at different temperatures. The end of the heating/cooling cycle is denoted as with an asterisk.

Temperature (°C)	Space Group	*a* (Å)	r_w (Å)
25	Pn3m	91.2 ± 0.6	18.6 ± 0.2
37	Pn3m	90 ± 1	18.1 ± 0.4
10	Pn3m	104 ± 1	23.8 ± 0.5
25*	Im3m	126 ± 2	22 ± 1
	Pn3m	95.0 ± 0.3	20.1 ± 0.1

due to the reduced thickness of the hydrophilic poly(methyl ethylene phosphate) corona surrounding the nanoparticles. When the system was heated back to 25 °C, the sample exhibits the coexistence of two phases: in addition to the native Pn3m, the Im3m bicontinuous cubic phase was observed, and the lattice parameter and water channel radius values evaluated from two peaks of such phase are in line with this finding [4,60]. Some hysteresis was observed for the position of the peaks of the Pn3m phase when the sample is heated again to standard temperature, with the lattice parameters and water channel radius slightly different from the samples measured directly at 25 °C before starting the temperature cycle. This phase transition followed by an equilibrium between the two phases is a common feature of cubosomes made of MO and Pluronics, and it is given rise from interactions between the stabilizer and the lipid bilayer. In this case, the lower degrees of freedom of the PPE polymer may lead to specific interactions with the bilayer, yielding the additional Im3m phase, as MO alone cannot form such phase at 10 °C [45,61]. These features could be relevant in terms of formulation storage.

Finally, the variation of D_h, PdI, and zeta potential of PS-Ru-loaded cubosomes as a function of the temperature were evaluated (Fig. 3D). The diameter at 25 °C is in line with those already evaluated for similar formulations [5,44,62], while the inclusion of PS-Ru leads to a slightly higher PdI. The zeta potential value does not seem to be significantly affected by the encapsulation of PS-Ru, suggesting that any physi-adsorption of such molecule should be excluded. When the system is heated to 37 °C, virtually no significant changes in terms or D_h, PdI and zeta potential were observed, being the different values within the experimental errors. On the other hand, the measurements at 10 °C highlighted a decrease in the hydrodynamic diameter of the cubosomes. Heating back the sample to 25 °C restores the size and zeta potential to the initial values.

In general, the formulation does not seem to be thermo-responsive, meaning that the balance of charge within the Stern layer does not change significantly upon increasing or decreasing the temperature. This indicates a strong colloidal stability, which was already highlighted by our previous investigation over time on the empty formulation [44].

Additionally, DLS and ELS analysis were carried over a 30-day period (Fig. S18) for a medium-term stability study of the colloidal systems stored at 25 °C. PS-RuCub optimal stability was revealed by the size distribution results, as evidenced by the average diameter that remained constant over the course of the storage period. The relatively narrow size distribution was also maintained, as evidenced by the nearly constant PdI values. A slight decrease of the zeta potential was observed after few weeks of storage, reaching values of approximately −30 mV after 30 days of monitoring. Such finding is in line with what already reported with the empty formulation [44].

3.3. Biological characterization of PS-Ru-loaded cubosomes

The anticancer potential of PS-Ru-loaded cubosomes was assessed in vitro, using a model of human lung adenocarcinoma and a LED array as illumination device. Being a newly synthesized complex, the photo-activity of PS-Ru (non-encapsulated) was initially evaluated. Briefly, two separate cell culture multiwell plates were employed for the test. After receiving the PS-Ru treatment in parallel, one plate was exposed to light for 30 min to trigger the photoactivation, while the other was kept in the dark for the same time. The cell viability determined 24 h after the treatment revealed a high photoactivity of PS-Ru coupled with substantial inertia in the dark (Fig. 4A). IC_{50} (half-maximal inhibitory concentration) values calculated for the two treatments, respectively equal to 0.0639 μM and > 25 μM, allowed to derive the phototoxic index (PI, defined as the ratio between IC_{50} in the dark/IC_{50} after irradiation) that exceeds 391. It needs to be noted that, in the concentration range tested, the exposure to PS-Ru in the dark never reduced the cell viability below the 50 %, not allowing the calculation of the IC_{50}, that is therefore reported as > 25 μM. The PI represents a quickly accessible and
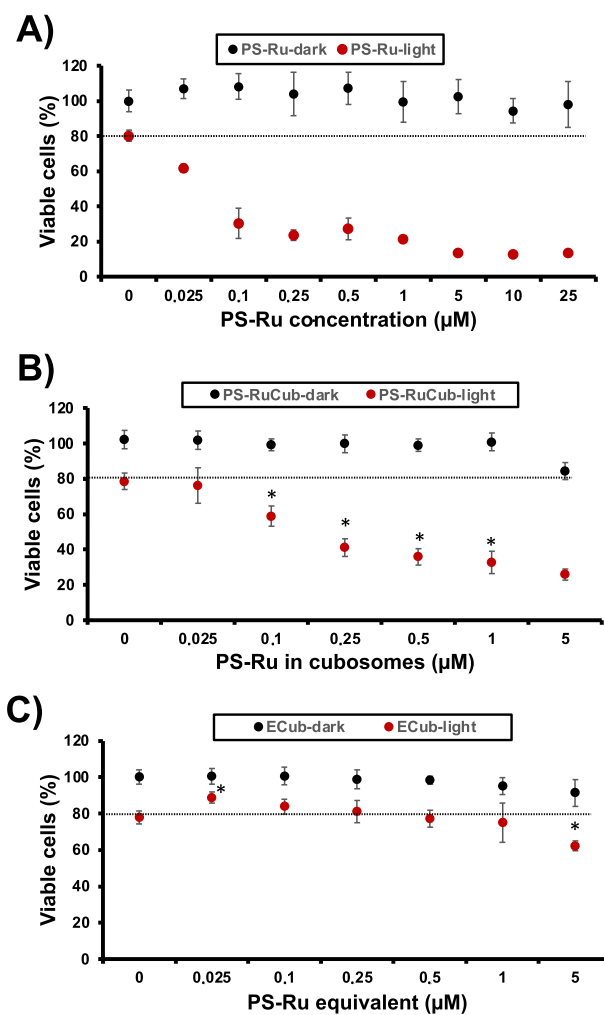

Fig. 4. Viability of Calu3 lung adenocarcinoma cells assessed by MTT following treatments with (A) the photosensitizer PS-Ru, (B) PS-Ru-loaded cubosomes (PS-RuCub), or (C) empty cubosomes (ECub), with or without exposure to light for 30 min. The dashed line is a guide for the eye to highlight the viability of cells exposed to light without PS. One way ANOVA with post-hoc Tukey HSD Test was employed to substantiate differences between cells only exposed to light (no PS-Ru, 0 μM) vs. cells treated with PS-RuCub or ECub and exposed to light (* $p < 0.01$) (n = 5).

informative parameter to rate the efficacy of a newly synthesized PS, with higher values being desirable to ensure high potency in target regions and minimum toxicity in the districts not subjected to irradiation. In the case of the PS-Ru presented in this work, the PI is in line with data from other analogues of the series, previously employed on a non-melanoma skin cancer model [48]. Focusing on the specific application for lung adenocarcinoma, our complex outperformed other Ru-based PS reported in literature, that showed PIs lower than 135 [63], 114 [64], and 50 [65]. On the other hand, in another recent report, a bimetallic Ru/Os complex triggering photodynamic and photothermal effects showed a remarkable PI of 821, suggesting that a combined mechanism allows to further increase the efficacy of these agents [66].

The next experiment followed the same protocol and was aimed at assessing the photoactivity/cytocompatibility of PS-RuCub. In this case as well, the phototoxic activity of PS-RuCub was distinctly observed, highlighting its responsiveness to light, while demonstrating negligible activity in the absence of light exposure (Fig. 4B). Not surprisingly, cubosomes encapsulation increases the IC_{50} of PS-Ru by approximately 2.2-fold (0.144 μM), while the IC_{50} value in the dark was > 5 μM. Such phenomenon is often observed when directly comparing free vs.

encapsulated drugs in vitro and is linked to the longer time required for endocytosis, intracellular processing, and drug release from the nanocarrier [67]. However, envisaging a clinical translation, nanoencapsulation of highly lipophilic PS allows to avoid the use of organic co-solvents (i.e., DMSO) for systemic administration, prolongs the circulation half-life, and might enhance tumor distribution through the Enhanced Permeability and Retention (EPR) effect. Combined together, these positive effects of nanoencapsulation (that would be explicitly appreciated in *in vivo* experiments) well counterbalance the observed reduction in efficacy, making cubosomes a convenient option for PS formulation and administration. The safety of the empty nanocarrier was then assessed to rule out any possible contribution of cubosomes components to the observed toxicity. Indeed, the use of PPE instead of Pluronic F127 as cubosome stabilizer already demonstrated lower toxicity and higher hemocompatibility, highlighting the translational potential of these delivery systems [44]. Here, unloaded cubosomes were confirmed to be safe, since only the highest concentration employed led to a mild but significant reduction in cell viability compared to control ($P < 0.01$, IC_{50} value after irradiation and in the dark always greater than 5 µM) (Fig. 4C).

Recent reports evidenced that cubosomes and similar liquid crystalline nanoparticles when exposed to biological media may undergo dynamic structural and morphological transformations, which also affect nanoparticle size distribution and number, presumably due to nanoparticles adsorption of plasma components and other environmental factors (e.g., ionic composition) [68]. Therefore, Ecub and PS-RuCub formulations were incubated for 1 h at 37 °C in the same medium used for the cell tests indicated in paragraph 2.14. Conditions (time of incubation, temperature, sample:medium ratio) were specifically chosen to reproduce those used for the in vitro tests. Following the incubation, the samples were measured via DLS and ELS (according to the procedure reported in the paragraph 2.12) to evaluate the stability of the cubosomes during the biological assays. Results are reported in Table 2. D_h and PdI values showed almost no discernible differences with data obtained in water. On the other hand, probably due to the higher ionic strength and composition of the medium, a decrease in the zeta potential values, equal to −17 mV for both samples, was observed. Consequently, the formulations can be considered stable under the

conditions used for the in vitro cell experiments.

PDT triggers cell death in vitro due to the production of ROS, that can in turn react with biological macromolecules activating the apoptotic cascade. Among the numerous effects of PDT on the cell homeostasis, alterations of the cell membrane are frequently observed [69]. Indeed, lipids composing the cell membrane are extremely sensitive to the oxidative stress triggered by PDT, that induces their peroxidation and the subsequent disruption of membrane-associated processes [70]. Membrane blebbing is a hallmark of cytoskeletal dysregulation and can be used as an accessible indicator of cells in the late stages of apoptosis. Here, light microscopy imaging allowed to observe the progressive formation of membrane blebs in cells treated with increasing concentrations of free PS-Ru (Fig. 5B,C) or with PS-RuCub (Fig. 5D) and exposed to light, highlighting cells undergoing apoptosis. Importantly, apoptosis is only one of the several possible mechanisms of cell death triggered by PDT, with other pathways involving other cell types (e.g., immunogenic cell death) playing an important role *in vivo* [71]. Conversely, the treatment of cells with empty cubosomes did not lead to any major morphological change (Fig. 5E), confirming the safety of the nanocarrier already observed with the metabolic tests.

4. Conclusions

The peculiar liquid-crystalline bicontinuous cubic nanostructure of cubosomes and their fusogenic properties [72] make these nanoparticles particularly appealing in pharmaceutical applications [73–76], and a number of different examples, involving all types of administration routes, are now available in literature [62,77,78]. However, the potency of cubosomes in PDT was only scarcely investigated so far, with only four papers reported in the literature [48,79–81]. Herein, in light of the encouraging results arising from the employment of RPCs-based photosensitizers in the photodynamic treatment of a wide variety of cancers, we explored the potential of cubosomes as nanocarriers for PS-Ru, a novel PS candidate belonging to a recently-developed class of RPCs-based PSs characterized by two π-extended dppn units simultaneously coordinated in their scaffolds. PS-Ru turned out to be a potent singlet oxygen sensitizer, with a quantum yield for singlet oxygen generation as high as 0.54 ± 0.06 in acetonitrile. The good singlet oxygen
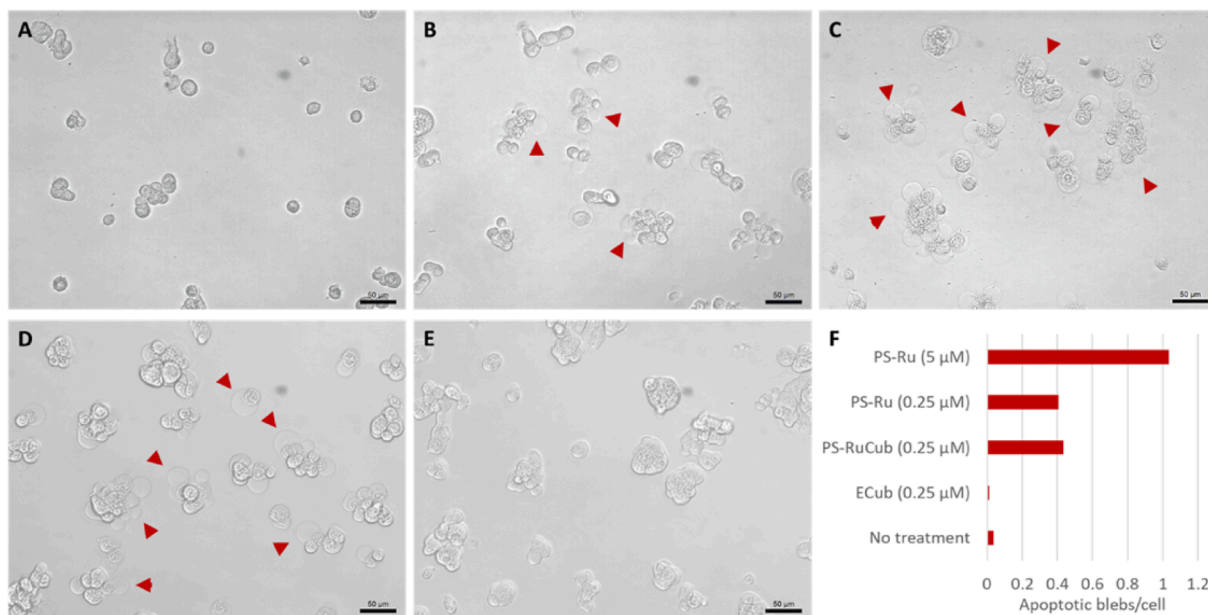

Fig. 5. Light microscopy images showing the morphology of Calu-3 cells after one hour exposure to no treatment (A), PS-Ru 0.25 µM (B), PS-Ru 5 µM (C), PS-RuCub 0.25 µM (D), or an equivalent volume of ECub (E) and 30 min LED irradiation (λ = 462 nm). Note the progressive granulation of cell bodies and the increasing number of apoptotic blebs (red arrowheads) when cells are subjected to PDT in vitro. Quantification of apoptotic blebs per cell in a defined area (0.22 mm^2) of the microscopy images (F). (For interpretation of the references to colour in this figure legend, the reader is referred to the web version of this article.)

sensitization capability was also paralleled by a potent phototoxic effect displayed in Calu3 lung adenocarcinoma cells, as witnessed by a PI index exceeding 391. With the goal of addressing key challenges hindering the use of PS in systemic administration, PS-Ru was then successfully encapsulated within the lipid bilayer of MO-based cubosomes stabilized with a highly biocompatible polyphosphoester analog of Pluronic F127. Our objective was to develop a PS formulation tailored for forthcoming *in vivo* tests in animal models. Although encapsulation into the cubosomes structure reduced the ability of the photosensitizer to trigger the formation of $^1O_2$, the PS-RuCub formulation still maintains an IC_{50} value after irradiation in the nM range, and the biological tests conclusively demonstrated the good phototoxic characteristics of the cubosomes formulation against lung adenocarcinoma cells under appropriate irradiation, simultaneously confirming its safety in the absence of light.

In conclusion, the design and successful implementation of the proposed nanoparticles emerges as a promising strategy to overcome the common drawbacks associated with RPCs, providing potential candidates for the preclinical development in the field of photodynamic therapy of lung adenocarcinoma.

CRediT authorship contribution statement

Luca Casula: Writing – original draft, Investigation. **Gina Elena Giacomazzo:** Investigation. **Luca Conti:** Writing – original draft, Investigation. **Marco Fornasier:** Writing – original draft, Investigation. **Benedetto Manca:** Visualization. **Michele Schlich:** Writing – original draft, Methodology, Investigation. **Chiara Sinico:** Writing – review & editing, Supervision, Conceptualization. **Timo Rheinberger:** Writing – original draft, Investigation. **Frederik R. Wurm:** Writing – review & editing, Supervision. **Claudia Giorgi:** Writing – review & editing, Supervision, Funding acquisition, Conceptualization. **Sergio Murgia:** Writing – review & editing, Writing – original draft, Supervision, Funding acquisition, Conceptualization.

Declaration of competing interest

The authors declare that they have no known competing financial interests or personal relationships that could have appeared to influence the work reported in this paper.

Data availability

Data will be made available on request.

Acknowledgments

Appendix A. Supplementary data

Supplementary data to this article can be found online at https://doi.org/10.1016/j.jcis.2024.05.088.

References

[1] S.B. Rizwan, B.J. Boyd, T. Rades, S. Hook, Bicontinuous cubic liquid crystals as sustained delivery systems for peptides and proteins, Expert Opin. Drug Deliv. 7 (2010) 1133–1144, https://doi.org/10.1517/17425247.2010.515584.

[2] S. Murgia, S. Lampis, P. Zucca, E. Sanjust, M. Monduzzi, Nucleotide Recognition and Phosphate Linkage Hydrolysis at a Lipid Cubic Interface, J. Am. Chem. Soc. 132 (2010) 16176–16184, https://doi.org/10.1021/ja1069745.

[3] H.M.G. Barriga, M.N. Holme, M.M. Stevens, Cubosomes: The Next Generation of Smart Lipid Nanoparticles? Angew. Chemie - Int. Ed. 58 (2019) 2958–2978, https://doi.org/10.1002/anie.201804067.

[4] S. Murgia, S. Biffi, R. Mezzenga, Recent advances of non-lamellar lyotropic liquid crystalline nanoparticles in nanomedicine, Curr. Opin. Colloid Interface Sci. 48 (2020) 28–39, https://doi.org/10.1016/j.cocis.2020.03.006.

[5] A. Yaghmur, H. Mu, Recent advances in drug delivery applications of cubosomes, hexosomes, and solid lipid nanoparticles, Acta Pharm. Sin. b. 11 (2021) 871–885, https://doi.org/10.1016/j.apsb.2021.02.013.

[6] A. Balestri, L. Gibot, H. Amenitsch, L. Cervelli, C. Montis, B. Lonetti, et al., PNIPAM-stabilized cubosomes as fusogenic delivery nanovectors for anticancer applications, Colloids Surfaces B Biointerfaces. 231 (2023) 113532, https://doi.org/10.1016/j.colsurfb.2023.113532.

[7] N.I. Zahid, M. Salim, C.Y. Liew, B.J. Boyd, R. Hashim, Structural investigation and steric stabilisation of Guerbet glycolipid-based cubosomes and hexosomes using triblock polyethylene oxide-polypropylene oxide-polyethylene oxide copolymers, Colloids Surfaces A Physicochem. Eng. Asp. 648 (2022) 129212, https://doi.org/10.1016/j.colsurfa.2022.129212.

[8] T. Rheinberger, O. Rabaux, C. Jérôme, F.R. Wurm, The future of polyphosphoesters, Eur. Polym. J. 200 (2023), https://doi.org/10.1016/j.eurpolymj.2023.112464.

[9] C. Pelosi, I. Constantinescu, H.H. Son, M.R. Tinè, J.N. Kizhakkedathu, F.R. Wurm, Blood Compatibility of Hydrophilic Polyphosphoesters, ACS Appl. Bio Mater. 5 (2022) 1151–1158, https://doi.org/10.1021/acsabm.1c01210.

[10] K.N. Bauer, L. Liu, M. Wagner, D. Andrienko, F.R. Wurm, Mechanistic study on the hydrolytic degradation of polyphosphates, Eur. Polym. J. 108 (2018) 286–294, https://doi.org/10.1016/j.eurpolymj.2018.08.058.

[11] J.H. Correia, J.A. Rodrigues, S. Pimenta, T. Dong, Z. Yang, Photodynamic therapy review: Principles, photosensitizers, applications, and future directions, Pharmaceutics. 13 (2021) 1332, https://doi.org/10.3390/pharmaceutics13091332.

[12] M. Ashrafizadeh, A. Zarrabi, H. Karimi-Maleh, A. Taheriazam, S. Mirzaei, M. Hashemi, et al., (Nano)platforms in bladder cancer therapy: Challenges and opportunities, Bioeng. Transl. Med. 8 (2023) e10353.

[13] L. Karner, S. Drechsler, M. Metzger, A. Hacobian, B. Schädl, P. Slezak, et al., Antimicrobial photodynamic therapy fighting polymicrobial infections-a journey from: In vitro to in vivo, Photochem. Photobiol. Sci. 19 (2020) 1332–1343, https://doi.org/10.1039/d0 pp00108b.

[14] G. Boccalini, L. Conti, C. Montis, D. Bani, A. Bencini, D. Berti, et al., Methylene blue-containing liposomes as new photodynamic anti-bacterial agents, J. Mater. Chem. b. 5 (2017) 2788–2797, https://doi.org/10.1039/c6tb03367a.

[15] M. Piksa, C. Lian, I.C. Samuel, K.J. Pawlik, I.D.W. Samuel, K. Matczyszyn, The role of the light source in antimicrobial photodynamic therapy, Chem. Soc. Rev. 52 (2023) 1697–1722, https://doi.org/10.1039/D0CS01051K.

[16] A.P. Castano, T.N. Demidova, M.R. Hamblin, Mechanisms in photodynamic therapy: part one—photosensitizers, photochemistry and cellular localization, Photodiagnosis Photodyn. Ther. 1 (2004) 279–293, https://doi.org/10.1016/S1572-1000(05)00007-4.

[17] S. Bonnet, Why develop photoactivated chemotherapy? Dalt. Trans. 47 (2018) 10330–10343, https://doi.org/10.1039/C8DT01585F.

[18] G.E. Giacomazzo, L. Conti, A. Guerri, M. Pagliai, C. Fagorzi, P.S. Sfragano, et al., Nitroimidazole-Based Ruthenium(II) Complexes: Playing with Structural Parameters to Design Photostable and Light-Responsive Antibacterial Agents, Inorg. Chem. 61 (2022) 6689–6694, https://doi.org/10.1021/acs.inorgchem.1c03032.

[19] G.E. Giacomazzo, L. Conti, C. Fagorzi, M. Pagliai, C. Andreini, A. Guerri, et al., Ruthenium(II) Polypyridyl Complexes and Metronidazole Derivatives: A Powerful Combination in the Design of Photoresponsive Antibacterial Agents Effective under Hypoxic Conditions, Inorg. Chem. 62 (2023) 7716–7727, https://doi.org/10.1021/acs.inorgchem.3c00214.

[20] G. Gunaydin, M.E. Gedik, S. Ayan, Photodynamic Therapy—Current Limitations and Novel Approaches, Front. Chem. 9 (2021), https://doi.org/10.3389/fchem.2021.691697.

[21] X. Deng, Z. Shao, Y. Zhao, Solutions to the Drawbacks of Photothermal and Photodynamic Cancer Therapy, Adv. Sci. 8 (2021) 2002504, https://doi.org/10.1002/advs.202002504.

[22] J.H. Sauraj, Oh. Kang, Y.T. Lee, Ko, Novel aggregation-induced emission-photosensitizers with built-in capability of mitochondria targeting and glutathione depletion for efficient photodynamic therapy, Nanoscale. 15 (2023) 4882–4892, https://doi.org/10.1039/D2NR06593B.

[23] L. Hang, T. Zhang, H. Wen, L. Liang, W. Li, X. Ma, et al., Controllable photodynamic performance via an acidic microenvironment based on two-dimensional metal-organic frameworks for photodynamic therapy, Nano Res. 14 (2021) 660–666, https://doi.org/10.1007/s12274-020-3093-1.

[24] A. George, P.S. Shrivastav, Photodynamic therapy with light emitting fabrics: a review, Arch. Dermatol. Res. 314 (2021) 929–936, https://doi.org/10.1007/s00403-021-02301-3.

[25] A.K. Singh, R. Malviya, S. Verma, Clinical Potential of Photodynamic Therapy in Skin Disorder, Infect. Disord. - Drug Targets. 23 (2022), https://doi.org/10.2174/1871526522666220907113617.

[26] L.C.C. Lee, K.K.W. Lo, Luminescent and Photofunctional Transition Metal Complexes: From Molecular Design to Diagnostic and Therapeutic Applications, J. Am. Chem. Soc. 144 (2022) 14420–14440, https://doi.org/10.1021/jacs.2c03437.

[27] S. Monro, K.L. Colón, H. Yin, J. Roque, P. Konda, S. Gujar, et al., Transition Metal Complexes and Photodynamic Therapy from a Tumor-Centered Approach:

Challenges, Opportunities, and Highlights from the Development of TLD1433, Chem. Rev. 119 (2019) 797–828, https://doi.org/10.1021/acs.chemrev.8b00211.

[28] L. Conti, A. Mengoni, G.E. Giacomazzo, L. Mari, M. Perfetti, C. Fagorzi, et al., Exploring the potential of highly charged Ru(II)- and heteronuclear Ru(II)/Cu(II)-polypyridyl complexes as antimicrobial agents, J. Inorg. Biochem. 220 (2021) 111467, https://doi.org/10.1016/j.jinorgbio.2021.111467.

[29] A. Notaro, G. Gasser, Monomeric and dimeric coordinatively saturated and substitutionally inert Ru(II) polypyridyl complexes as anticancer drug candidates, Chem. Soc. Rev. 46 (2017) 7317–7337, https://doi.org/10.1039/c7cs00356k.

[30] L. Conti, G.E. Giacomazzo, B. Valtancoli, M. Perfetti, A. Privitera, C. Giorgi, et al., Highly Charged Ru(II) Polypyridyl Complexes as Photosensitizer Agents in Photodynamic Therapy of Epithelial Ovarian Cancer Cells, Int. J. Mol. Sci. 23 (2022) 13302, https://doi.org/10.3390/ijms232113302.

[31] M. Verrucchi, G.E. Giacomazzo, P.S. Sfragano, S. Laschi, L. Conti, M. Pagliai, et al., Characterization of a Ruthenium(II) Complex in Singlet Oxygen-Mediated Photoelectrochemical Sensing, Langmuir. 39 (2023) 679–689, https://doi.org/10.1021/acs.langmuir.2c03042.

[32] L. Conti, E. Macedi, C. Giorgi, B. Valtancoli, V. Fusi, Combination of light and Ru (II) polypyridyl complexes: Recent advances in the development of new anticancer drugs, Coord. Chem. Rev. 469 (2022) 214656, https://doi.org/10.1016/j.ccr.2022.214656.

[33] S.P. Foxon, C. Metcalfe, H. Adams, M. Webb, J.A. Thomas, Electrochemical and Photophysical Properties of DNA Metallo-intercalators Containing the Ruthenium (II) Tris(1-pyrazolyl)methane Unit, Inorg. Chem. 46 (2007) 409–416, https://doi.org/10.1021/ic0607134.

[34] P.M. de Groot, C.C. Wu, B.W. Carter, R.F. Munden, The epidemiology of lung cancer, Transl. Lung. Cancer Res. 7 (2018) 220–233, https://doi.org/10.21037/tlcr.2018.05.06.

[35] A. Crous, H. Abrahamse, Photodynamic therapy of lung cancer, where are we? Front. Pharmacol. 13 (2022) 1–13, https://doi.org/10.3389/fphar.2022.932098.

[36] A.G. Nicholson, M.S. Tsao, M.B. Beasley, A.C. Borczuk, E. Brambilla, W.A. Cooper, et al., The 2021 WHO Classification of Lung Tumors: Impact of Advances Since 2015, J. Thorac. Oncol. 17 (2022) (2021) 362–387, https://doi.org/10.1016/j.jtho.2021.11.003.

[37] C.B. Tripathi, S. Mukherjee, Lewis base catalysis by thiourea: N-bromosuccinimide-mediated oxidation of alcohols, J. Org. Chem. 77 (2012) 1592–1598, https://doi.org/10.1021/jo202269p.

[38] S. Schöttler, G. Becker, S. Winzen, T. Steinbach, K. Mohr, K. Landfester, et al., Protein adsorption is required for stealth effect of poly(ethylene glycol)- and poly (phosphoester)-coated nanocarriers, Nat. Nanotechnol. 11 (2016) 372–377, https://doi.org/10.1038/nnano.2015.330.

[39] Z. Molphy, A. Prisecaru, C. Slator, N. Barron, M. McCann, J. Colleran, et al., Copper phenanthrene oxidative chemical nucleases, Inorg. Chem. 53 (2014) 5392–5404, https://doi.org/10.1021/ic500914j.

[40] P.A. Anderson, G.B. Deacon, K.H. Haarmann, F. Richard Keene, T.J. Meyer, D.A. Reitsma, et al., Designed Synthesis of Mononuclear Tris(heteroleptic) Ruthenium Complexes Containing Bidentate Polypyridyl Ligands, Inorg. Chem. 34 (1995) 6145–6157, https://doi.org/10.1021/ic00128a028.

[41] M. Kubeil, R.R. Vernooij, C. Kubeil, B.R. Wood, B. Graham, H. Stephan, et al., Studies of Carbon Monoxide Release from Ruthenium(II) Bipyridine Carbonyl Complexes upon UV-Light Exposure, Inorg. Chem. 56 (2017) 5941–5952, https://doi.org/10.1021/acs.inorgchem.7b00599.

[42] R. Roy, J.M. Kim, Cu(II)-Self-assembling bipyridyl-glycoclusters and dendrimers bearing the Tn-antigen cancer marker: syntheses and lectin binding properties, Tetrahedron. 59 (2003) 3881–3893, https://doi.org/10.1016/S0040-4020(03)00438-1.

[43] L. Conti, A. Bencini, C. Ferrante, C. Gellini, P. Paoli, M. Parri, et al., Highly Charged Ruthenium(II) Polypyridyl Complexes as Effective Photosensitizer in Photodynamic Therapy, Chem. – A Eur. J. 25 (2019) 10606–10615, https://doi.org/10.1002/chem.201901570.

[44] M. Fornasier, S. Biffi, B. Bortot, P. Macor, A. Manhart, F.R. Wurm, et al., Cubosomes stabilized by a polyphosphoester-analog of Pluronic F127 with reduced cytotoxicity, J. Colloid Interface Sci. 580 (2020) 286–297, https://doi.org/10.1016/j.jcis.2020.07.038.

[45] C.V. Kulkarni, W. Wachter, G. Iglesias-Salto, S. Engelskirchen, S. Ahualli, Monoolein: A magic lipid? Phys. Chem. Chem. Phys. 13 (2011) 3004–3021, https://doi.org/10.1039/c0cp01539c.

[46] A.H. Shoen, Infinite periodic minimal surfaces without self-intersections, NASA Tech, Note. (1970) D-5541.

[47] I. Wolfram Research, Mathematica, Version 14 (2024). https://www.wolfram.com/mathematica.

[48] G.E. Giacomazzo, M. Schlich, L. Casula, L. Galantini, A. Del Giudice, G. Pietraperzia, et al., Ruthenium(ii) polypyridyl complexes with π-expansive ligands: synthesis and cubosome encapsulation for photodynamic therapy of non-melanoma skin cancer, Inorg. Chem. Front. 10 (2023) 3025–3036, https://doi.org/10.1039/d2qi02678c.

[49] A. Notaro, M. Jakubaszek, S. Koch, R. Rubbiani, O. Dömötör, É.A. Enyedy, et al., A Maltol-Containing Ruthenium Polypyridyl Complex as a Potential Anticancer Agent, Chem. – A Eur. J. 26 (2020) 4997–5009, https://doi.org/10.1002/chem.201904877.

[50] E. Wachter, D.K. Heidary, B.S. Howerton, S. Parkin, E.C. Glazer, Light-activated ruthenium complexes photobind DNA and are cytotoxic in the photodynamic therapy window, Chem. Commun. 48 (2012) 9649–9651, https://doi.org/10.1039/c2cc33359g.

[51] M.J. Nickita, A.I. Belousoff, A.M. Bhatt, G.B. Bond, G.G. Deacon, et al., Synthesis, Structure, Spectroscopic Properties, and Electrochemical Oxidation of Ruthenium (II) Complexes Incorporating Monocarboxylate Bipyridine Ligands, Inorg. Chem. 46 (2007) 8638–8651, https://doi.org/10.1021/ic700796m.

[52] B. Peña, N.A. Leed, K.R. Dunbar, C. Turro, Excited state dynamics of two new Ru (II) cyclometallated dyes: Relation to cells for solar energy conversion and comparison to conventional systems, J. Phys. Chem. c. 116 (2012) 22186–22195, https://doi.org/10.1021/jp306352f.

[53] H.K. Saeed, P.J. Jarman, S. Archer, S. Sreedharan, I.Q. Saeed, L.K. Mckenzie, et al., Homo- and Heteroleptic Phototoxic Dinuclear Metallo-Intercalators Based on Ru II (dppn) Intercalating Moieties: Synthesis, Optical, and Biological Studies, Angew, Chemie. 129 (2017) 12802–12807, https://doi.org/10.1002/ange.201707350.

[54] M.D. Pozza, P. Mesdom, A. Abdullrahman, T.D. Prieto Otoya, P. Arnoux, C. Frochot, et al., Increasing the π-Expansive Ligands in Ruthenium(II) Polypyridyl Complexes: Synthesis, Characterization, and Biological Evaluation for Photodynamic Therapy Applications, Inorg. Chem. 62 (2023) 18510–18523, https://doi.org/10.1021/acs.inorgchem.3c02606.

[55] M.S. Baptista, J. Cadet, P. Di Mascio, A.A. Ghogare, A. Greer, M.R. Hamblin, et al., Type I and Type II Photosensitized Oxidation Reactions: Guidelines and Mechanistic Pathways, Photochem. Photobiol. 93 (2017) 912–919, https://doi.org/10.1111/php.12716.

[56] X. Mulet, X. Gong, L.J. Waddington, C.J. Drummond, Observing self-assembled lipid nanoparticles building order and complexity through low-energy transformation processes, ACS Nano. 3 (2009) 2789–2797, https://doi.org/10.1021/nn900671u.

[57] D. Demurtas, P. Guichard, I. Martiel, R. Mezzenga, C. Hebert, L. Sagalowicz, Direct visualization of dispersed lipid bicontinuous cubic phases by cryo-electron tomography, Nat. Commun. 6 (2015) 8915, https://doi.org/10.1038/ncomms9915.

[58] M. Fornasier, S. Murgia, Non-lamellar lipid liquid crystalline nanoparticles: A smart platform for nanomedicine applications, Front, Soft Matter. 3 (2023) 1–13, https://doi.org/10.3389/frsfm.2023.1109508.

[59] I.D. Azmi, S.M. Moghimi, A. Yaghmur, Cubosomes and hexosomes as versatile platforms for drug delivery, Ther. Deliv. 6 (2015) 1347–1364, https://doi.org/10.4155/tde.15.81.

[60] C. Oliveira, C.J.O. Ferreira, M. Sousa, J.L. Paris, R. Gaspar, B.F.B. Silva, et al., A Versatile Nanocarrier — Cubosomes, Characterization, and Applications, Nanomaterials. 12 (2022) 1–26, https://doi.org/10.3390/nano12132224.

[61] H. Qiu, M. Caffrey, The phase diagram of the monoolein/water system: Metastability and equilibrium aspects, Biomaterials. 21 (2000) 223–234, https://doi.org/10.1016/S0142-9612(99)00126-X.

[62] Y. Mohammad, R.N. Prentice, B.J. Boyd, S.B. Rizwan, Comparison of cubosomes and hexosomes for the delivery of phenytoin to the brain, J. Colloid Interface Sci. 605 (2022) 146–154, https://doi.org/10.1016/j.jcis.2021.07.070.

[63] Y. Wang, P.S. Felder, P. Mesdom, O. Blacque, T.L. Mindt, K. Cariou, et al., Towards Ruthenium(II)-Rhenium(I) Binuclear Complexes as Photosensitizers for Photodynamic Therapy, ChemBioChem. 24 (2023) 1–10, https://doi.org/10.1002/cbic.202300467.

[64] Z. Zhou, J. Liu, T.W. Rees, H. Wang, X. Li, H. Chao, et al., Heterometallic Ru–Pt metallacycle for two-photon photodynamic therapy, Proc. Natl. Acad. Sci. u. s. a. 115 (2018) 5664–5669, https://doi.org/10.1073/pnas.1802012115.

[65] X. Ma, J. Lu, P. Yang, Z. Zhang, B. Huang, R. Li, et al., 8-Hydroxyquinoline-modified ruthenium(ii) polypyridyl complexes for JMJD inhibition and photodynamic antitumor therapy, Dalt. Trans. 51 (2022) 13902–13909, https://doi.org/10.1039/d2dt01765b.

[66] Y.A. Deng, S.J. Tang, M.F. Wang, X. Ren, X.L. Li, L.Z. Zeng, et al., Heterometallic ruthenium-osmium complexes: dual photodynamic and photothermal therapy for melanoma and drug-resistant lung tumour in vivo, Inorg. Chem. Front. 10 (2023) 4552–4561, https://doi.org/10.1039/d3qi00903c.

[67] A. Felici, M. Schlich, D. Di Mascolo, L. Goldoni, A. Lisa Palange, P. Decuzzi, Boosting the therapeutic efficacy of discoidal nanoconstructs against glioblastoma with rationally designed PEG-Docetaxel conjugates, Eur. J. Pharm. Biopharm. 174 (2022) 90–100, https://doi.org/10.1016/j.ejpb.2022.03.011.

[68] A. Yaghmur, S.M. Moghimi, Intrinsic and Dynamic Heterogeneity of Nonlamellar Lyotropic Liquid Crystalline Nanodispersions, ACS Nano. 17 (2023) 22183–22195, https://doi.org/10.1021/acsnano.3c09231.

[69] E. Panzarini, B. Tenuzzo, L. Dini, Photodynamic therapy-induced apoptosis of HeLa cells, Ann. n. y. Acad. Sci. 1171 (2009) 617–626, https://doi.org/10.1111/j.1749-6632.2009.04908.x.

[70] H. Hiruma, T. Katakura, T. Takenami, S. Igawa, M. Kanoh, T. Fujimura, et al., Vesicle disruption, plasma membrane bleb formation, and acute cell death caused by illumination with blue light in acridine orange-loaded malignant melanoma cells, J. Photochem. Photobiol. B Biol. 86 (2007) 1–8, https://doi.org/10.1016/j.jphotobiol.2006.08.003.

[71] T. Mishchenko, I. Balalaeva, A. Gorokhova, M. Vedunova, D.V. Krysko, Which cell death modality wins the contest for photodynamic therapy of cancer? Cell Death Dis. 13 (2022) 1–16, https://doi.org/10.1038/s41419-022-04851-4.

[72] C.P. Pilkington, C. Contini, J.D. Barritt, P.A. Simpson, J.M. Seddon, Y. Elani, A microfluidic platform for the controlled synthesis of architecturally complex liquid crystalline nanoparticles, Sci. Rep. 13 (2023) 1–14, https://doi.org/10.1038/s41598-023-39205-3.

[73] X. Lai, M.L. Han, Y. Ding, S.H. Chow, A.P. Le Brun, C.M. Wu, et al., A polytherapy based approach to combat antimicrobial resistance using cubosomes, Nat. Commun. 13 (2022) 1–12, https://doi.org/10.1038/s41467-022-28012-5.

[74] H. Yu, J.S. Palazzolo, Y. Ju, B. Niego, S. Pan, C.E. Hagemeyer, et al., Polyphenol-Functionalized Cubosomes as Thrombolytic Drug Carriers, Adv. Healthc. Mater. 11 (2022) 1–14, https://doi.org/10.1002/adhm.202201151.

[75] S. Sarkar, B. Dyett, B. Lakic, A.S. Ball, L.Y. Yeo, J.F. White, et al., Cubosome Lipid Nanocarriers As a Drug Delivery Vehicle for Intracellular Mycobacterium tuberculosis Infections, ACS Appl. Mater. Interfaces. 15 (2023) 21819–21829, https://doi.org/10.1021/acsami.3c00101.

[76] M. Zabara, B. Senturk, M. Gontsarik, Q. Ren, M. Rottmar, K. Maniura-Weber, et al., Multifunctional Nano-Biointerfaces: Cytocompatible Antimicrobial Nanocarriers from Stabilizer-Free Cubosomes, Adv. Funct. Mater. 29 (2019), https://doi.org/10.1002/adfm.201904007.

[77] S. Subramaniam, P. Joyce, L. Donnellan, C. Young, A. Wignall, P. Hoffmann, et al., Protein adsorption determines pulmonary cell uptake of lipid-based nanoparticles, J. Colloid Interface Sci. 641 (2023) 36–47, https://doi.org/10.1016/j.jcis.2023.03.048.

[78] B.V. Pimenta, R.R.M. Madrid, P.D. Mathews, K.A. Riske, W. Loh, B. Angelov, et al., Interaction of polyelectrolyte-shell cubosomes with serum albumin for triggering drug release in gastrointestinal cancer, J. Mater. Chem. b. 11 (2023) 2490–2503, https://doi.org/10.1039/d2tb02670h.

[79] U. Bazylińska, D. Wawrzyńczyk, J. Kulbacka, G. Picci, L.S. Manni, S. Handschin, et al., Hybrid Theranostic Cubosomes for Efficient NIR-Induced Photodynamic Therapy, ACS Nano. 16 (2022) 5427–5438, https://doi.org/10.1021/acsnano.1c09367.

[80] U. Bazylińska, J. Kulbacka, J. Schmidt, Y. Talmon, S. Murgia, Polymer-free cubosomes for simultaneous bioimaging and photodynamic action of photosensitizers in melanoma skin cancer cells, J. Colloid Interface Sci. 522 (2018) 163–173, https://doi.org/10.1016/j.jcis.2018.03.063.

[81] S. Jenni, G. Picci, M. Fornasier, M. Mamusa, J. Schmidt, Y. Talmon, et al., Multifunctional cubic liquid crystalline nanoparticles for chemo- A nd photodynamic synergistic cancer therapy, Photochem. Photobiol. Sci. 19 (2020) 674–680, https://doi.org/10.1039/c9 pp00449a.